Available online at www.sciencedirect.com
ScienceDirect
International Journal of Thermal Sciences 46 (2007) 38–47
International Journal of Thermal Sciences
www.elsevier.com/locate/ijts

Lattice Boltzmann method applied to the laminar natural convection in an enclosure with a heat-generating cylinder conducting body

Mohammed Jami [a], Ahmed Mezrhab [a,*], M'hamed Bouzidi [b], Pierre Lallemand [c]

[a] *Faculté des Sciences, Département de Physique, Université Mohamed I, Oujda, Morocco*
[b] *Université Clermont-2, IUT Ave A. Briand, 03100 Montluçon, France*
[c] *LIMSI, Bâtiment 508, Université Paris-Sud, 91405 Orsay, France*

Received 19 August 2005; received in revised form 18 January 2006; accepted 17 March 2006

Available online 11 July 2006

Abstract

In this paper, a numerical investigation of laminar convective flows in a differentially heated, square enclosure with a heat-conducting cylinder at its center, is carried out. The flow and the temperature are computed using respectively the lattice Boltzmann equation and finite-difference with suitable coupling to take natural convection into account. The investigation is performed for $Pr = 0.71$, Rayleigh numbers of $Ra = 10^3$–10^6 and temperature-difference ratio of $\Delta T^* = 0$–50. The average hot and cold walls Nusselt numbers, the flow and temperature fields are presented and discussed. For a constant Ra, the average Nusselt number at the hot and cold walls (Nu_h and Nu_c) vary linearly with ΔT^*: Nu_h decreases with ΔT^* while Nu_c increases with ΔT^*.

PACS: 44.25i.+f; 47.11i.+j

Keywords: Natural convection; Lattice Boltzmann method; Heat generation; Inner body; Average Nusselt number

1. Introduction

Thermal transfers are needed in modern technology and are very important in many industrial areas. Hence it is necessary to study and simulate these phenomena. Several numerical and experimental methods have been developed to investigate enclosures with and without obstacle because these geometries have great practical engineering applications. House et al. [1] studied the effect of a centered, square, heat conducting body on natural convection in a vertical enclosure. They have shown that heat transfer across the cavity may be enhanced or reduced by a body with a thermal conductivity ratio smaller or greater than unity. They also found that the heat transfer can be minimal as the size of the body is increased. The same geometry was reported in the numerical study of Oh et al. [2] when a conducting body generates heat within the enclosure. In this study, it is shown that the flow is driven by a temperature difference across the enclosure and a temperature difference caused by the heat source. They demonstrated a transition from a flow dominated by the temperature difference across the enclosure to that dominated by the temperature difference due to the heat transfer. Ha et al. [3] investigated the unsteady natural convection process of three different fluids: sodium, air, and water in a differentially heated square cavity within which a centered, square, heat-conducting body generates heat. They studied with respect to the dimensionless time, the effects of the Prandtl number, the thermal conductivity ratio, the heat capacity ratio, and the temperature-difference ratio on variations of streamlines, isotherms and the average Nusselt numbers at hot and cold walls. Ha et al. [4] investigated the steady, three-dimensional heat transfer and flow characteristics of natural convection in a vertical cubic enclosure differentially heated inside which a cubic body generates heat. They found that the flow and isotherm distributions show very complex three-dimensional patterns. Mezrhab et al. [5] studied the radiation-natural convection interactions in a differ-

* Corresponding author. Tel.: +212 56 50 06 01/02; fax: +212 56 50 06 03.
E-mail addresses: m.jami@sciences.univ-oujda.ac.ma (M. Jami), mezrhab@sciences.univ-oujda.ac.ma (A. Mezrhab), bouzidi@asci.fr (M. Bouzidi), lalleman@asci.fr (P. Lallemand).

1290-0729/$ – see front matter
doi:10.1016/j.ijthermalsci.2006.03.010

Nomenclature

A	cavity aspect ratio ($A = H/L = 1$)	
A_b	body area, πr^2	m^2
g	acceleration of gravity	$m\,s^{-2}$
H	enclosure height	m
k	thermal conductivity	$W\,m^{-1}\,K^{-1}$
L	enclosure width	m
Nu	average wall Nusselt number, $\frac{-1}{\Delta T}\int_0^H \left(\frac{\partial T}{\partial x}\right)_{\text{wall}} dy$	
Pr	Prandtl number, ν/α_f	
q_b	heat generation per unit volume	$W\,m^{-3}$
r	radius of the cylinder	m
Ra	Rayleigh number, $g\beta\Delta T L^3/\nu\alpha_f$	
R_k	thermal conductivity ratio, k_b/k_f	
R_α	thermal diffusivity ratio, α_b/α_f	
T	temperature	K
T_0	average fluid temperature, $(T_h + T_c)/2$	K
u	x velocity component	$m\,s^{-1}$
v	y velocity component	$m\,s^{-1}$
x, y	Cartesian coordinates	m

Greek symbols

α	thermal diffusivity	$m^2\,s^{-1}$
β	volumetric expansion coefficient	K^{-1}
ΔT	maximal temperature difference, $T_h - T_c$	K
ΔT^*	temperature-difference ratio, $(q_b A_b)/(k_b \Delta T)$	
$\Delta T_0{}^*$	temperature-difference ratio at which the average hot wall Nusselt number is equal to zero	
ν	kinematic viscosity of the fluid, Eq. (5)	$m^2\,s^{-1}$
ψ	stream function	$m^2\,s^{-1}$
Ψ	dimensionless stream function, ψ/α_f	
$\Psi_{\max}$	maximum dimensionless stream function	
θ	dimensionless temperature, $(T - T_0)/\Delta T$	

Subscripts

b	inner body
c	cold wall
f	fluid
h	hot wall

entially heated square cavity within which a centered, square, heat-conducting body generates heat. For the solution of the governing equations, they have used a specifically developed numerical model based on the finite-volume method and the SIMPLER algorithm. They have found that:

(i) the isotherms and streamlines are strongly affected by the radiation exchange at high Rayleigh numbers ($Ra \geqslant 10^6$),
(ii) the temperature of the inner body decreases owing to the radiation exchange effect,
(iii) for a fixed Ra, the average Nusselt number at the hot and cold walls (Nu_h and Nu_c) vary linearly with increasing ΔT^*.

Numerically, the classical methods are based on the resolution of the Navier–Stokes equations. These methods rest on the spatial and temporal discretization of the macroscopic evolution equations. A different mesoscopic approach (lattice Boltzmann method) may be used to simulate the fluid flow. This method is based on a simplification of the Boltzmann equation considered in the kinetic theory of gases. As discussed in the next section, it can be coupled to a standard numerical scheme for the evolution of the temperature (for instance a simple finite-difference scheme) to provide a convenient way to simulate thermo-convective problems. This is used in several recent papers [6,7] including our previous work [8]. For the convection cases considered in this previous work, we found that the coupled LBE-FD method is a robust second-order numerical technique that can deal easily with boundaries of various shapes and properties. Other authors [7] have come to similar conclusions. In this study, we propose to use a numerical coupling between the lattice Boltzmann equation in its refined multi-relaxation approach [10] and finite difference method to obtain the velocity and temperature fields. This paper is organized as follows: Section 2 reviews the numerical analysis (lattice Boltzmann equation and energy equation), Section 3 presents the code validation, Section 4 discusses the results and the last section concludes the paper.

2. Numerical analysis

Natural convection in cavities including a partition or an inner body have been investigated by several authors; however the inner body has generally a square shape [1–5]. In this study we consider the configuration that is shown in Fig. 1. The horizontal walls are perfectly insulated while the two vertical walls are maintained at two different temperature T_h and T_c respectively. The fluid moves inside the cavity due to the buoyancy force generated by the density gradients. The working fluid is Newtonian and incompressible;[1] viscous dissipation is neglected in the energy equation and it is assumed that the Boussinesq approximation is applicable. Differing from previous studies, the inner body considered in this work is a conducting cylinder which generates heat.

2.1. Lattice Boltzmann equation

The origin of lattice Boltzmann equation (LBE) is the lattice gas automaton (LGA) model proposed by Frisch et al. [9] together with the standard description of gases in kinetic theory with a velocity distribution function $f(\mathbf{r}, \mathbf{v}, t)$ that depends on space, velocity and time and is a Maxwellian distribution for

[1] The LBE technique is intrinsically compressible but departure from true incompressible flows are of the order of the square of the fluid velocity, hence conditions are chosen such that the maximum speed in the cavity is below 0.1 in non-dimensional units of the LBE algorithm.

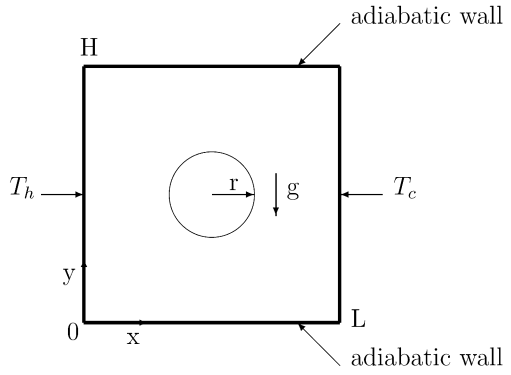

Fig. 1. Square cavity simulated.

a uniform gas at equilibrium. The basic idea of the LBE technique (see Ref. [11] for a review) is to consider f at discrete points of a highly symmetric lattice (usually square or cube), for discrete times $t_l = l\tau$ and for a small number of velocities chosen such they correspond to motions from lattice nodes to close-by lattice nodes during one time step (of duration τ). If the set of velocities for which f is defined has $b+1$ elements $\mathbf{c}_0, \mathbf{c}_i$, $i \in \{1, \ldots, b\}$, then we consider that for each node $\mathbf{r}$ of the lattice and each time t_l, the system is completely defined by the set of $b+1$ real numbers $f_i(\mathbf{r}, l)$, $i \in \{0, \ldots, b\}$. It is convenient to consider a $b+1$ component vector

$$F = \{f_0, f_1, \ldots, f_b\}^{\mathrm{T}} \tag{1}$$

As we describe here results for 2-D situations, we take the simple D2Q9 model with 9 velocities, in this case $b = 8$.

The dynamics of the system follows the lattice Boltzmann equation

$$f_i(\mathbf{x} + \mathbf{c}_i, t+1) = f_i(\mathbf{x}, t) + (\Omega F)_i \tag{2}$$

This can be interpreted as follows: a time step of duration 1 (in normalized time units) can be split in two substeps. One represented by the operator Ω that acts to redistribute the f_i at each lattice node corresponds to "collisions", the other one (change of node and change of time) corresponds to advection (or motion from lattice nodes to other lattice nodes). Note that if the basic velocities $\mathbf{c}_i$ are adequately chosen the advection substep is exact. Approximations with respect to real physics are used to simplify the operator Ω. In the early work on LBE only the result $(\Omega F)_i$ was given for particularly simple forms of the collision operator (LBE-BGK case). However it turns out that it is preferable in terms of stability of the technique and a broader choice in the macroscopic properties of the model to use the so-called LBE-MRT (multi relaxation time) version [10]. This is what we do here. In the LBE-MRT approach, the state of the system at each lattice node is represented by the vector F and a set of moments that is derived from F by a linear transformation

$$M = \{m_0, m_1, \ldots, m_b\}^{\mathrm{T}} = AF \tag{3}$$

The choice of the (non-singular) matrix A follows what is done in kinetic theory of gases and takes advantage of the symmetries of the problem. It is convenient that the density (sum of the f_i) and the flux of momentum be included in M. In the LBE-MRT approach the advection substep of Eq. (2) is performed in F space, whereas the collision substep is performed in M space. For simplicity the collision step is defined as a linear relaxation of moments towards their equilibrium value, following the set of equations that applies for all moments that are modified in collisions (that is other than density and Cartesian components of the momentum for Navier–Stokes or than the density if one wishes to simulate the diffusion equation),

$$m_j^{\mathrm{ac}} = m_j^{\mathrm{bc}} + s_j\left(m_j^{\mathrm{eq}} - m_j^{\mathrm{bc}}\right) \tag{4}$$

where m_j^{ac} is the moment after collision, m_j^{bc} is the moment before collision, m_j^{eq} is the equilibrium values of the non-conserved moments and it can be chosen at will provided that the symmetry of the problem is respected [8,12], and s_j is a relaxation rate. For stability reasons s_j must be taken between 0 and 2. It can be shown that the kinematic viscosity of the system is given by:

$$\nu = 1/3(1/s_{XY} - 1/2) \tag{5}$$

where s_{XY} is the relaxation rate of the off-diagonal stress tensor. It is beyond the scope of this paper to present an analysis of the LBE technique and of the accuracy of its predictions for simple situations using techniques used for instance in Ref. [12]. We just indicate that we used for the relaxation rates of the non-conserved moments {1.4, 1.4, 1.2, 1.2} respectively for {kinetic energy, square of kinetic energy, x and y components of the flux of energy}. These values are not critical unless one wishes to simulate conditions for large fluid velocity and/or use a limited number of grid points to represent the smallest scales of the flow under study.[2]

2.1.1. Boundary conditions

The introduction of boundaries is done in the following way. We apply the usual bounce-back condition [14] at all solid cavity walls which are thus located with a good approximation in between the last "fluid" node and the first "solid" point. On the inner interfaces (fluid/inner body), the boundary conditions are applied using a combination of the bounce-back scheme and of spatial quadratic interpolation [15,16]. The justification for using interpolation is that the distribution function f_i are smooth continuous in both space and time. There are some particles that are going to be in interstitial positions after being rebounded by the inner body. This is the reason why we used this combination. This technique is graphically depicted in Fig. 2. The bounce-back boundary conditions place the physical wall at the half grid spacing beyond the last fluid node x_f; but there are others cases when this wall is not located at this distance. In fact we define the parameter q that expresses the fraction in fluid region of a grid spacing intersected by the boundary, i.e., $q \equiv |x_f - x_w|/\delta_x$. In Fig. 2(a) it is clear that the particle moves

[2] Note that free parameters in the LBE model can be tuned to increase stability at large speed or to increase the accuracy at short spatial scale and that the optimal values are not the same for the two cases. Making a reasonable choice is therefore left to the initiative of the user of LBE.

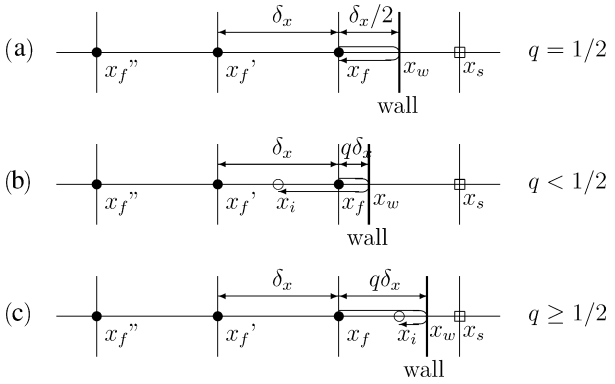

Fig. 2. Illustration of the boundary conditions for a rigid wall located between two grid sites in the direction of the movement of the particle that is rebounded.

from x_f toward x_w, then it comes back to its place after being reflected by the wall. This case is submitted to the usual bounce-back boundary conditions. Whereas in the two others cases Fig. 2(b) and (c), the particle stands in interstitial positions x_i. To keep the structure of the grid, the distribution must be reconstructed. For example in case of $q < 1/2$. At time t the distribution function of the particle with velocity pointing to the wall (Fig. 2(b)) at the grid point x_f (a fluid node) would end up at the point x_i located at a distance $(1-2q)\delta_x$ away from the grid point x_f, after the bounce-back collision. Because x_i is not a grid point, the value of f_3 at the grid point x_f needs to be reconstructed. Noticing that f_1 starting from point x_i would become f_3 at the grid point x_f after the bounce-back collision with the wall, we construct the values of f_1 at the point x_i by a quadratic interpolation involving values of f_1 at the three locations: $f_1(x_f)$, $f_1(x_f{}') = f_1(x_f - c_1)$ and $f_1(x_f{}'') = f_1(x_f - 2c_1)$. In a similar manner, for the case of $q \geqslant 1/2$, we can construct $f_3(x_f)$ by a quadratic interpolation involving $f_3(x_f)$ that is equal to $f_1(x_f)$ before the bounce-back collision, and the values of f_3 at the nodes after collision and advection, i.e., $f_3(x_f{}')$, and $f_3(x_f{}'')$. Therefore the interpolations are applied differently for the two cases:

(1) For $q < 1/2$, interpolate before propagation and bounce-back collision.
(2) For $q \geqslant 1/2$, interpolate after propagation and bounce-back collision.

We do so to avoid the use of extrapolations in the boundary conditions for the sake of numerical stability. This leads to the following interpolation formulas (where the notations $\hat{f}_i$ and f_i denote the post-collision distribution functions before and after advection):

$$f_{\bar{i}}(x_f,t) = q(1+2q)\,\hat{f}_i(x_f,t) + (1-4q^2)\,\hat{f}_i(x_f{}',t) - q(1-2q)\,\hat{f}_i(x_f{}'',t) \quad q < 1/2 \tag{6}$$

$$f_{\bar{i}}(x_f,t) = \frac{1}{q(1+2q)}\,\hat{f}_i(x_f,t) + \frac{(2q-1)}{q}\,f_{\bar{i}}(x_f{}',t) - \frac{(2q-1)}{(2q+1)}\,f_{\bar{i}}(x_f{}'',t) \quad q \geqslant 1/2 \tag{7}$$

where $f_{\bar{i}}$ is the distribution function of the velocity $c_{\bar{i}} \equiv -c_i$. Note that if one uses an efficient LBE code in which collisions and motions are performed together, then the information needed in the previous equations are moved one step along c_i so the effect of boundaries is taken care of by:

$$f_{\bar{i}}(x_f,t) = q(1+2q)\,f_i(x_f+c_i,t) + (1-4q^2)\,f_i(x_f,t) - q(1-2q)\,f_i(x_f-c_i,t) \tag{8}$$

$$f_{\bar{i}}(x_f,t) = \frac{1}{q(1+2q)}\,f_i(x_f+c_i,t) + \frac{(2q-1)}{q}\,f_{\bar{i}}(x_f-c_i,t) - \frac{(2q-1)}{(2q+1)}\,f_{\bar{i}}(x_f-2c_i,t) \tag{9}$$

2.2. Equation of temperature

The dimensionless temperature θ provides a buoyancy force in the y direction, $f_y = g\beta\Delta T\theta(\mathbf{r},t)$, where $\mathbf{r}$ is the position of the air node which has temperature $\theta(\mathbf{r},t)$ at time t. The usual LBE analysis of the long time, large spatial scale behavior leads to "Navier–Stokes"-like equations with the adequate coupling between the temperature field and the hydrodynamical variables, and unmodified expressions for the viscosity. As far as the energy equation is concerned, several schemes were considered for the time integration: alternating-directional implicit (ADI) splitting scheme [13] simple explicit Euler scheme, Heun's method (second-order predictor-corrector), the last one giving a very good compromise between accuracy and computational efficiency so that the time spent solving the energy equation could be as small as 1/5 of the time spent solving the LBE part of the computation, due in part to the fact that we could take a time step for the energy equation larger than the time step used for LBE. Using the dimensionless temperature θ, the energy equation can be expressed by the following two-dimensional equation:
For the fluid region:

$$\frac{\partial\theta}{\partial t} + u\frac{\partial\theta}{\partial x} + v\frac{\partial\theta}{\partial y} = \alpha_f\left(\frac{\partial^2\theta}{\partial x^2} + \frac{\partial^2\theta}{\partial y^2}\right) \tag{10}$$

For the solid body region:

$$\frac{\partial\theta}{\partial t} = R_\alpha\alpha_f\left[\left(\frac{\partial^2\theta}{\partial x^2} + \frac{\partial^2\theta}{\partial y^2}\right) + \frac{\Delta T^*}{A_b}\right] \tag{11}$$

At the fluid-body interface, the boundary thermal conditions are:

$$\theta_b = \theta_f; \quad R_k\frac{\partial\theta_b}{\partial n} = \frac{\partial\theta_f}{\partial n} \tag{12}$$

where n denotes the normal direction to the interface under consideration.

If $N_x \times N_y = N^2$ is the number of fluid points in the numerical grid ($N_x = N_y = N$), according to the bounce-back boundary condition and LBE techniques [14], the effective boundaries

will be at $1/2$ and $N + 1/2$. We may use for the finite difference scheme the same grid points as for the LBE scheme. In that case, we must therefore use as boundary conditions for the temperature.

$$\theta(1/2, y) = \theta_h = 0.5 \qquad \text{for } \tfrac{1}{2} \leqslant y \leqslant N + \tfrac{1}{2}$$
$$\theta(N + 1/2, y) = \theta_c = -0.5 \qquad \text{for } \tfrac{1}{2} \leqslant y \leqslant N + \tfrac{1}{2}$$
$$\frac{\partial\theta}{\partial y}(x, 1/2) = 0 \qquad \text{for } \tfrac{1}{2} \leqslant x \leqslant N + \tfrac{1}{2}$$
$$\frac{\partial\theta}{\partial y}(x, N + 1/2) = 0 \qquad \text{for } \tfrac{1}{2} \leqslant x \leqslant N + \tfrac{1}{2}$$

On the enclosure walls and on the body $u = v = 0$.

3. Code validation

The numerical code used for the present study was rigorously verified. In the cases of an empty cavity, a square cavity with a hot circle inside, and concentric cylinders, the presented numerical study was checked for accuracy against the earlier published numerical and experimental results reported by different authors, and the agreement between the present and previous results was very good in Ref. [8]. In this paper, we present a comparison between the results given by our calculation and those reported in the bibliography [1,2,5]. The physical problem studied by these authors is a vertical square enclosure with sides of length L. The vertical walls are isothermal and differentially heated, whereas the bottom and top walls are adiabatic. This enclosure is centered by a square, heat-conducting body with sides of length equal to $L/2$. The grid size used is 121×121 in the x and y directions, respectively. For the same parameters used in Ref. [1,2,5] and without heat generated by the inner body, Table 1 shows the average wall Nusselt number comparison.

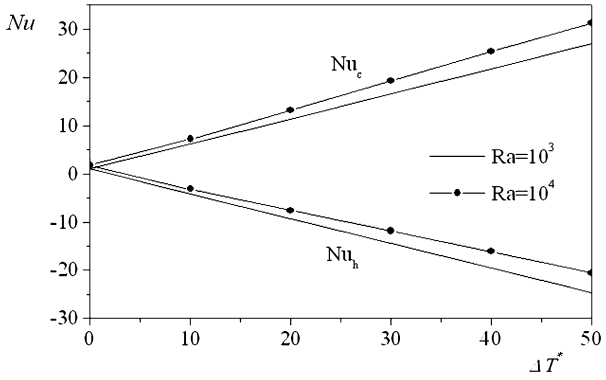

Fig. 3. Variation of the average wall Nusselt number with ΔT^* for $Pr = 0.71$ and $R_k = 1$.

Table 1
Comparison of the average wall Nusselt number for $R_k = 1$, $\Delta T^* = 0$ and $Pr = 0.71$

Ra	*Nu*			
	Present	Oh et al. [2]	House et al. [1]	Mezrhab et al. [5]
10^3	1.015	1.016	no data	1.016
10^4	1.759	1.770	no data	1.766
10^5	4.467	no data	4.506	4.458

Fig. 3 presents a graphical comparison concerning the variation of the average Nusselt numbers at the hot and cold walls as a function of the temperature-difference ratios ΔT^*. In the same way, Fig. 4 presents the streamlines and the isotherms. We note an excellent agreement between our results shown in Figs. 3 and 4 and those obtained, in Figs. 4 and 6 of Oh et al. [2]. The largest discrepancies between the present results and those reported in [1,2,5] can be estimated to be less than 1 per cent.

4. Results and discussions

Numerical simulations are performed for $A = 1$, $Pr = 0.71$, $r = H/6$, $R_k = 1$, $R_\alpha = 1$, $10^3 \leqslant Ra \leqslant 10^6$ and $0 \leqslant \Delta T^* \leqslant 50$. In order to examine the influence of Ra and ΔT^* upon the flow and temperature field inside the enclosure, we first varied the mesh size to determine the optimum uniform grid (i.e. the best compromise between accuracy and computational costs). Then, we have considered the following case: $Pr = 0.71$, $Ra = 10^6$ and $\Delta T^* = 50$, to compute $\Psi_{\max}$ and Nu for each grid size. As can be seen in Fig. 5, the relative differences between the results obtained for 121×121 and 161×161 grid points are below 1% for $\Psi_{\max}$ and less than 6×10^{-3} for Nu. Consequently, for most of the computations reported in this study a grid with 121×121 was chosen to optimise the relation between the

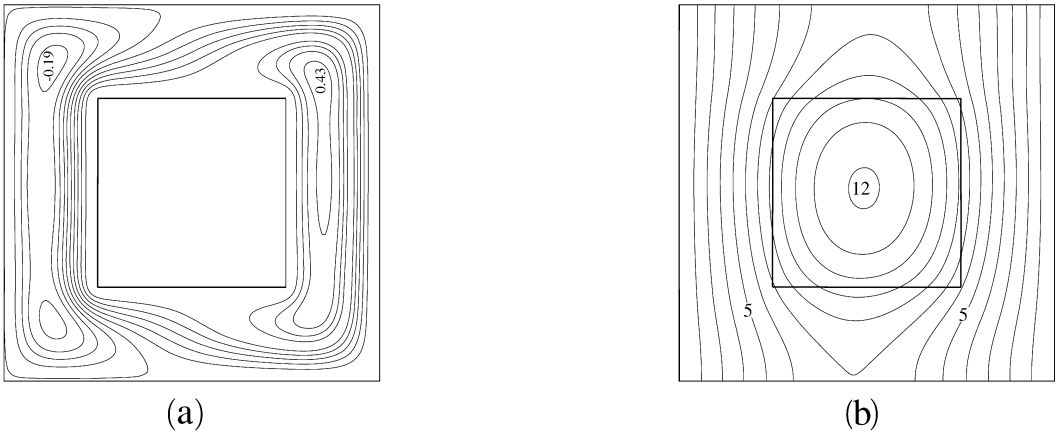

Fig. 4. Isograms at $Ra = 10^3$, $R_k = 1$, $Pr = 0.71$ and $\Delta T^* = 50$: (a) streamlines; (b) isotherms.

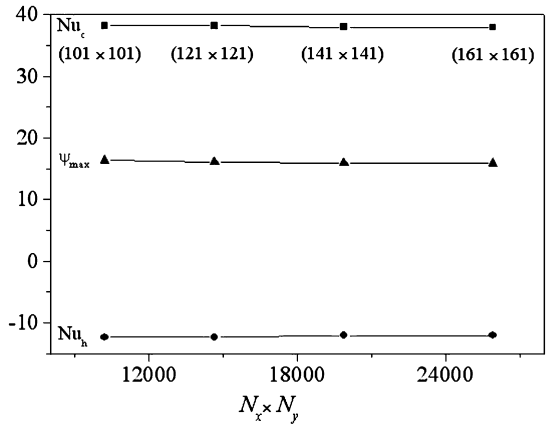

Fig. 5. The influence of the mesh size on the accuracy of the results for $Pr = 0.71$, $Ra = 10^6$ and $\Delta T^* = 50$.

required accuracy and the computing time. The isotherms are plotted using the dimensionless temperature θ. The dimensionless stream function Ψ is defined as usual through $u = \alpha_f(\frac{\partial \Psi}{\partial y})$ and $v = -\alpha_f(\frac{\partial \Psi}{\partial x})$. The number of contour lines is fixed to 11 for all isotherm plots and to 14 for all streamline plots with the same step in each case.

4.1. Isotherms and streamlines

The isotherms and streamlines are shown in Figs. 6–9 for a Rayleigh number of 10^3–10^6. For each value of *Ra*, the temperature-difference ratios equal to: 0, 10 and 50. When the inner body does not generate heat ($\Delta T^* = 0$), the streamlines circulate in the clockwise direction owing to the positions of the cold and hot walls. At low values of *Ra*, the air circula-

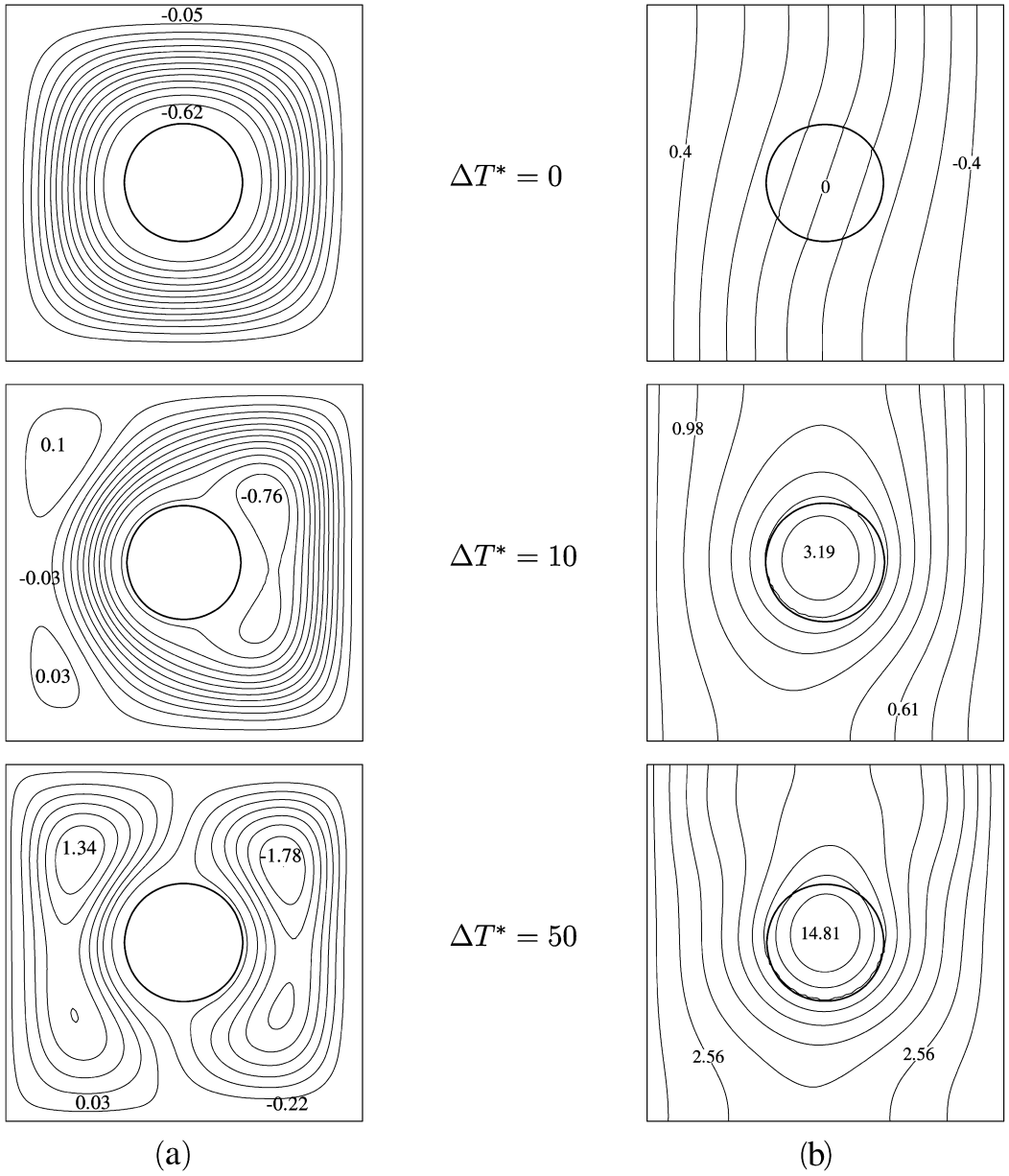

Fig. 6. Isograms at $Ra = 10^3$: (a) streamlines; (b) isotherms.

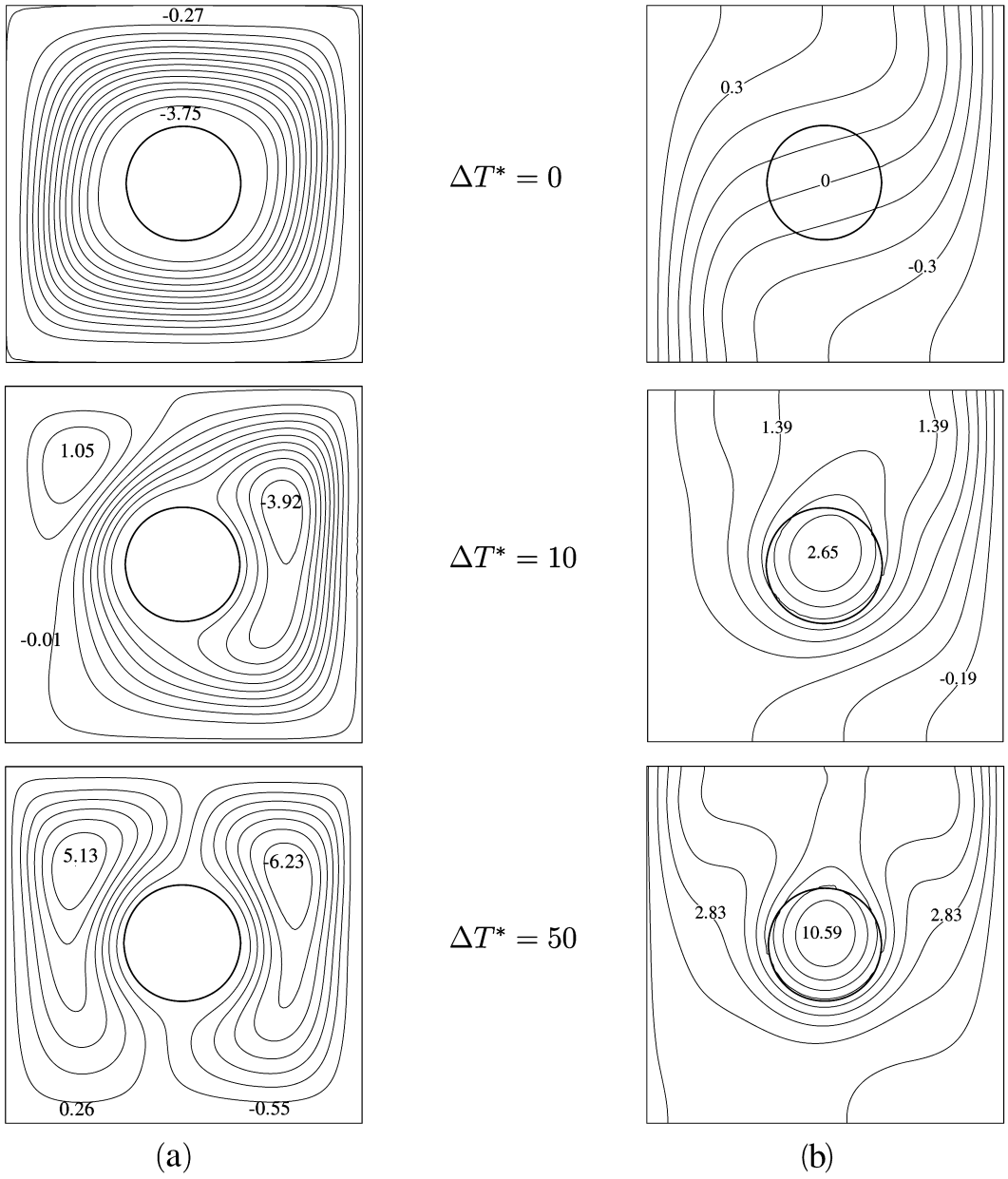

Fig. 7. Isograms at $Ra = 10^4$: (a) streamlines; (b) isotherms.

tion is weaker, the streamlines are circular and the isotherms appear to be nearly parallel to the active walls because the heat transfer mode is conduction. When *Ra* increases, the flow velocity increases and it causes a stronger circulation near the hot and cold walls. The isotherms move in the clockwise direction and become almost horizontal in the inner body, indicating that heat is conducted vertically through the body, from the higher temperature fluid in the upper part of the cavity to the lower temperature fluid in the lower part. When the inner body generates heat ($\Delta T^* \neq 0$), we note an increase of the temperature inside the enclosure, and the maximum temperature at the body is higher than the one of the hot wall. The heat generated by the body influences the shapes of the isotherms, and it is transferred to the fluid that carry it to the cold wall. However, in the left region of the cavity, the heat transferred from the body to the fluid increases its temperature which becomes greater than that of the hot wall. Thus, heat is transferred from the fluid to the hot wall. This behavior causes a second circulation in the counter-clockwise direction in this region. This circulation becomes larger when ΔT^* increases. As ΔT^* increases further, the fluid temperature next to the hot wall becomes hotter and, for a certain ΔT^*, the average hot wall Nusselt number becomes zero. Above this temperature-difference ratio, a fraction of the heat generated by the body moves out through the hot wall. The temperature inside the enclosure decreases with increasing *Ra*, because the convective heat transfer increases i.e. the air velocity increases and therefore the inner body loses more energy by convection. The point of maximum temperature for $Ra = 10^3$ is located almost at the center of the body, whereas the one for $Ra > 10^4$ is at the upper part of the vertical center-

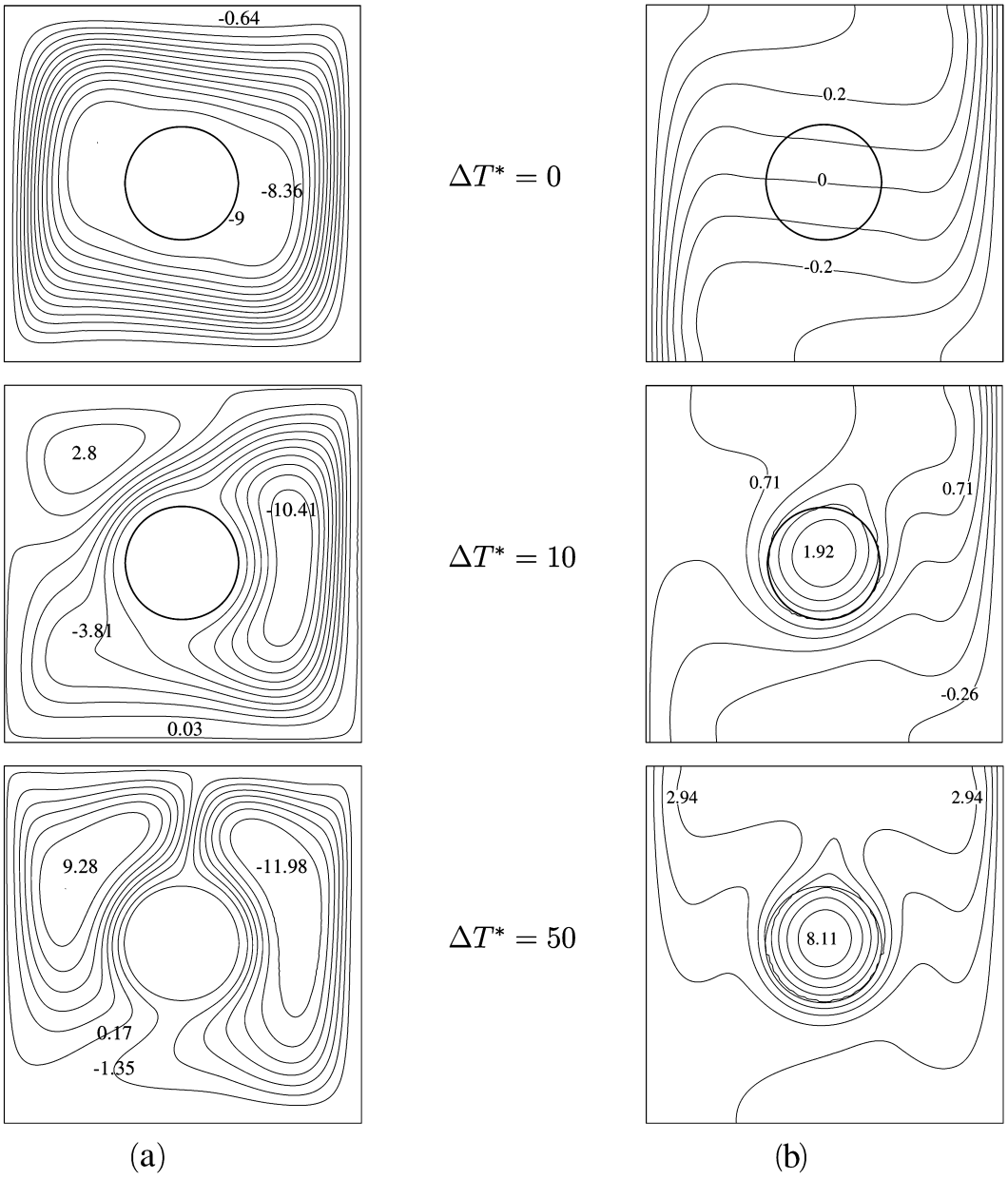

Fig. 8. Isograms at $Ra = 10^5$: (a) streamlines; (b) isotherms.

line owing to the asymmetric temperature fields. For $\Delta T^* \geqslant 30$, the heat generated by the inner body is considerable, which causes an increase of the temperature in the enclosure and the isotherms become almost symmetrical across the vertical centerline. Indeed, at high value of ΔT^*, the surface temperatures of the inner body are much greater than those of the isothermal walls and the problem becomes as if these walls were maintained to the same temperature.

4.2. Average wall Nusselt number

The variation of the average Nusselt numbers of the hot and cold walls vs Rayleigh number, for $0 \leqslant \Delta T^* \leqslant 50$, is depicted in Fig. 10. With increasing *Ra*, both hot and cold walls Nusselt numbers increase. This is due to the increase of the buoyancy force. Except the case of $Nu_h = Nu_c$, the profiles are parallel because ΔT^* varies by the same step that is equal to 10. On the other hand, for a fixed value of *Ra*, Nu_c increases, but Nu_h decreases with increasing ΔT^*. This is clearly represented in Figs. 11(a) and (b) showing the average Nusselt number at the hot and cold walls for various temperature-difference ratios and for $Ra = 10^3, 10^4$ and $Ra = 10^5, 10^6$, respectively. The variation of both Nu_h and Nu_c is linear. From Figs. 11(a) and (b), we can deduce ${\Delta T_0}^*$, at which the average hot wall Nusselt number Nu_h becomes zero. We find that ${\Delta T_0}^*$ increases with increasing *Ra* from 10^3 to 10^6, resulting in increasing convection effect which gives an increase in both Nu_c and Nu_h, meaning that the circulating flow in the cavity increases and more heat is transferred to the cold wall or to the ambient through the hot wall. Due to this behavior, the average cold wall Nusselt number for

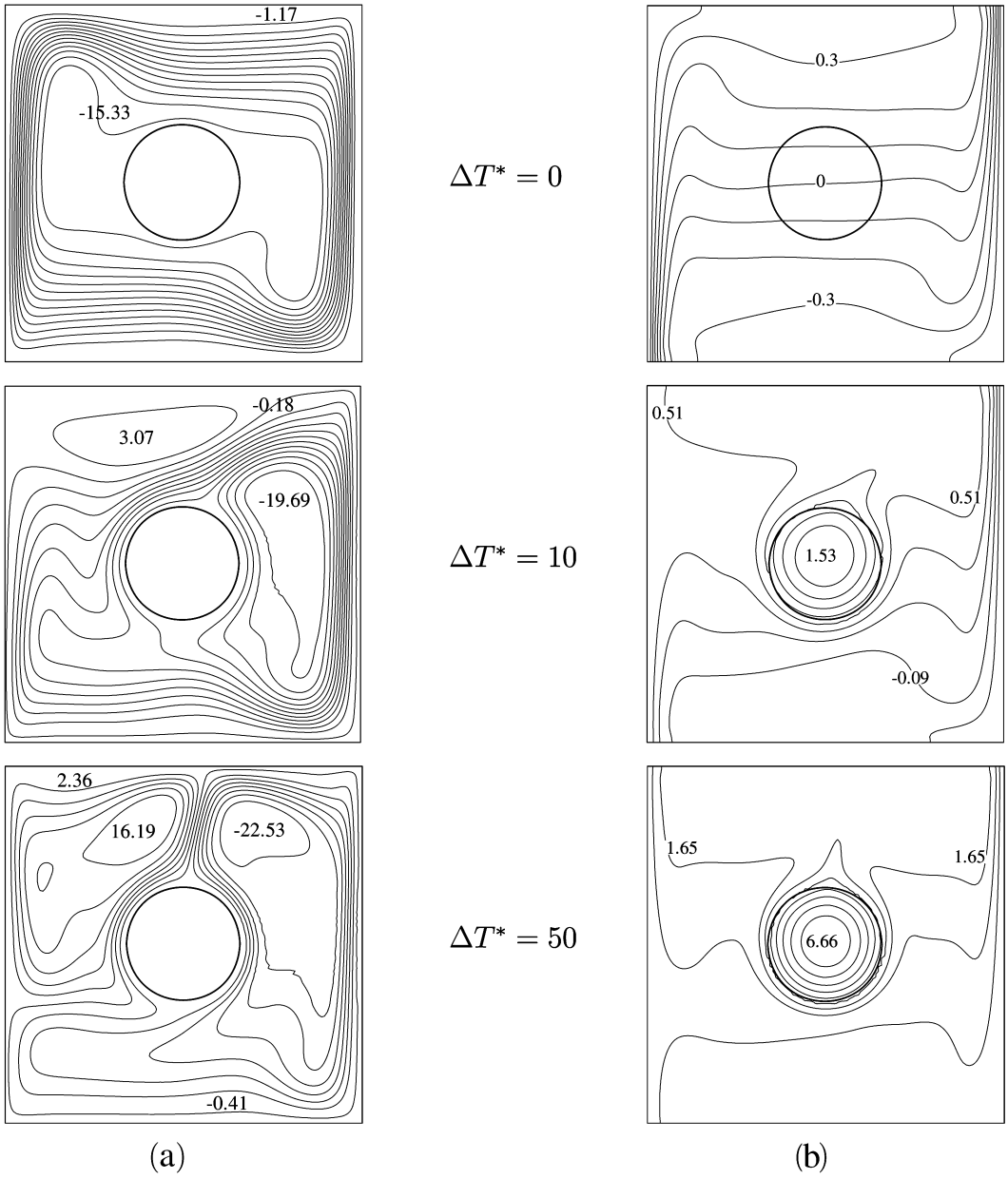

Fig. 9. Isograms at $Ra = 10^6$: (a) streamlines; (b) isotherms.

high *Ra* increases more quickly than that for low *Ra*, while the average hot wall Nusselt number for high *Ra* decreases more slowly than that for low *Ra*. Nu_c and the absolute value of Nu_h increase linearly with increasing ΔT^* but, the increase of Nu_c is important with respect to the one of the absolute value of Nu_h owing to the air temperature which becomes high in the right part of the cavity. According to the energy conservation, the difference between Nu_c and Nu_h is equal to ΔT^*, hence:

$$\Delta T^* = Nu_c - Nu_h \tag{13}$$

5. Conclusion

Natural convection in a differentially heated enclosure, within which a centered, circular, heat-conducting body generates heat, was successfully solved numerically through the

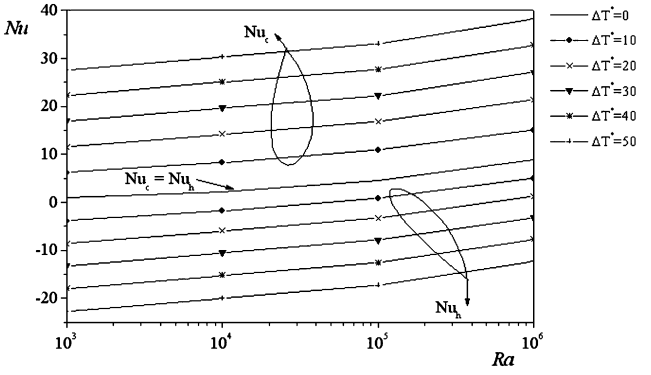

Fig. 10. Variation of the average wall Nusselt number with *Ra* for ΔT^* varying from 0 to 50.

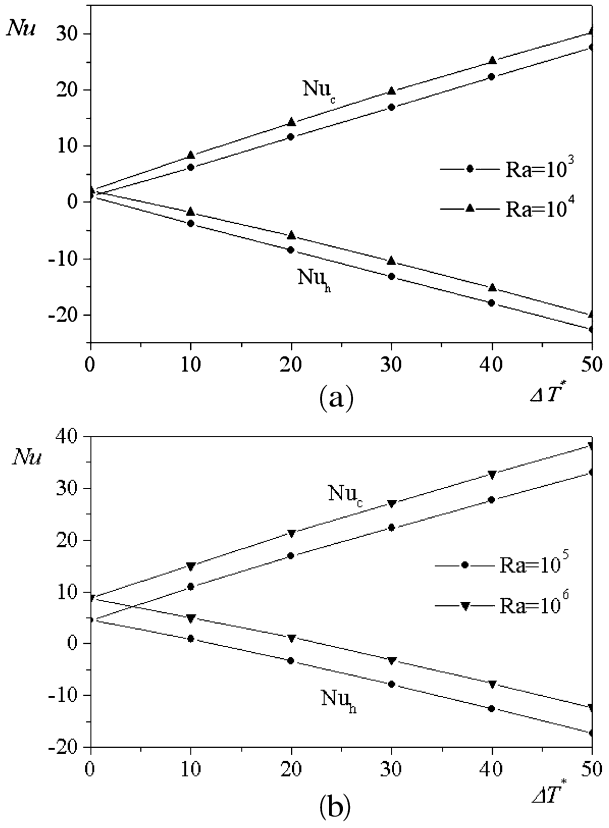

Fig. 11. Variation of the average wall Nusselt number with ΔT^*: (a) $Ra = 10^3$ and 10^4; (b) $Ra = 10^5$ and 10^6.

FD-LBE coupling. For the Rayleigh number ranging between 10^3 and 10^6, and for temperature-difference ratio varying from 0 to 50, the main results obtained may be summarized as follows:

(1) For a constant Ra, the average Nusselt number at the hot (cold) wall decreases (increases) linearly with increasing ΔT^*. When $\Delta T^* < \Delta T_0{}^*$, Nu_h is positive and the net heat transfer at the hot wall is into the fluid of the enclosure. At $\Delta T^* = \Delta T_0{}^*$, the net heat transfer at the hot wall becomes zero, whereas at $\Delta T^* > \Delta T_0{}^*$, it is negative, and it is transferred out of the fluid.
(2) The relation binding the average Nusselt numbers at the hot and cold walls, and the temperature-difference ratio is $\Delta T^* = Nu_c - Nu_h$.
(3) Independently of the value of ΔT^*, the maximal temperature in the cavity decreases with increasing Ra.
(4) For $\Delta T^* \geqslant 40$, the heat transfer and the air flow in the cavity are under the quasi-total dominance of the heat generated by the inner body.

Finally, the results obtained in a two-dimensional configuration are very interesting and can have important implications in several industrial applications. However, the three-dimensional simulations are more realistic, particularly when the inner body does not spread to the whole depth of the cavity. Therefore, our perspective is to simulate in a three-dimensional case, the natural convection in a rectangular cavity with a heat-generating conducting body.

References

[1] J.M. House, C. Beckermann, T.F. Smith, Effect of a centered conducting body on natural convection heat transfer in an enclosure, Numerical Heat Transfer, Part A 18 (1990) 213–225.
[2] J.Y. Oh, M.Y. Ha, Y.S. Kim, Numerical study of heat transfer and flow of natural convection in an enclosure with a heat-generating conducting body, Numerical Heat Transfer, Part A 31 (1997) 289–304.
[3] M.Y. Ha, M.J. Jung, Y.S. Kim, A numerical study on transient heat transfer and fluid flow of natural convection in an enclosure with a heat-generating conducting body, Numerical Heat Transfer, Part A 35 (1999) 415–434.
[4] M.Y. Ha, M.J. Jung, A numerical study on three-dimensional conjugate heat transfer of natural convection and conduction in a differentially heated cubic enclosure with a heat-generating cubic conducting body, International Journal of Heat and Mass Transfer 43 (2000) 4229–4248.
[5] A. Mezrhab, H. Bouali, C. Abid, Modelling of combined radiative and convective heat transfer in an enclosure with a heat-generating conducting body, International Journal of Computational Methods 2 (3) (2005) 431–450.
[6] X. Shan, Simulation of Rayleigh–Bénard convection using a lattice Boltzmann method, Physical Review E 55 (1997) 2780–2788.
[7] X. He, S. Chen, G.D. Doolen, A novel thermal model for the lattice Boltzmann method in incompressible limit, Journal of Computational Physics 146 (1998) 282–300.
[8] A. Mezrhab, M. Bouzidi, P. Lallemand, Hybrid lattice Boltzmann finite-difference simulation of convective flows, Computer and Fluids 33 (2004) 623–641.
[9] U. Frisch, D. Hasslacher, P. Lallemand, Y. Pomeau, J.P. Rivet, Lattice gas hydrodynamics in 2 and 3 dimensions, Complex Systems 1 (1987) 648.
[10] D. d'Humières, Generalized lattice Boltzmann equations, in: B.D. Shizgal, D.P. Weaver (Eds.), Rarefied Gas Dynamics Theory and Simulations, in: Progress in Astronautics and Aeronautics, vol. 159, AIAA, Washington, DC, 1992.
[11] S. Chen, G.D. Doolen, Lattice Boltzmann method for fluid flows, Annual Review of Fluid Mechanics 30 (1998) 329–364.
[12] P. Lallemand, L.S. Luo, Theory of the lattice Boltzmann method: dispersion, dissipation, isotropy, Galilean invariance and stability, Physical Review E 61 (2000) 6546–6562.
[13] P.J. Roache, Computational Fluid Dynamics, revised ed., Hermosa, Albuquerque, New Mexico, 1982.
[14] I. Ginzbourg, P.M. Adler, Boundary flow condition analysis for the three-dimensional lattice Boltzmann model, Journal de Physique Paris II 4 (1994) 191–214.
[15] M. Bouzidi, M. Firdaouss, P. Lallemand, Momentum transfer of a Boltzmann lattice fluid with boundaries, Physics of Fluids 13 (2001) 3452–3459.
[16] P. Lallemand, L.S. Luo, Lattice Boltzmann method for moving boundaries, Journal of Computational Physics 184 (2003) 406–421.